



Rotating Detonation Combustor Downstream Transition Passage Design Considerations

James Braun¹(✉), Guillermo Paniagua¹, and Donald Ferguson²

¹ Purdue University, West Lafayette, IN, USA

² NETL, Morgantown, WV, USA

Abstract. A key enabler to integrate turbines downstream of rotating detonation combustors is the design of an optimal combustor-turbine passage. Precise estimates of fluctuations, losses, and heat loads are required for the turbine design as rotating detonation combustors feature transonic flow with rotating shocks moving at few kilohertz. This paper analyzes fluctuations and heat loads of the Purdue Turbine Integrated high-Pressure RDE through reactive unsteady Reynolds Averaged Navier-Stokes (URANS) simulations. CFD++, a commercial CFD software package from Metacomp, is employed to solve the unsteady RANS equations through a one-step reaction mechanism. The inlet of the combustor is fed with a hydrogen-air mixture at mass flows of ~1 kg/s with two different back pressures to obtain supersonic and subsonic outlet flows. The mesh featured around 36 million grid points to ensure the resolving of the boundary layer. Finally, a methodology to lower computational time tenfold for the supersonic and subsonic passage is presented based on non-reacting unsteady RANS simulations.

Keywords: Rotating detonation combustors · Supersonic passage · Subsonic passage

1 Introduction

Rotating detonation combustors (RDCs) are a promising technology for power generation [1]. However, the gains of RDCs are accompanied by supersonic rotating shock waves with large fluctuations in Mach number, flow angle, pressure, and temperature [2]. In the past decade, significant efforts have been attributed to the understanding of combustors; literature from Anand et al. [3] and Ma et al. [4] provide a review of the operability of RDEs. Early on, Euler solvers were employed to understand their flow field [5], followed by three-dimensional Reynolds-averaged Navier-Stokes solvers [6] with induction parameter models, one-step and multi-step reaction mechanisms [7], and more recently Large Eddy Simulations through Converge CFD [8] with 21 species, 38 reactions reaction mechanisms for ethylene air are employed or through opensource OpenFoam flow solvers [9]. Experimental validation of pressure gain is performed through total pressure measurements [6] or equivalent available pressure with choked back-pressured RDCs [10].

While some researchers have focused on nozzle guide vanes on the combustor (Asli et al. [11]) other teams have focused on optimizing the turbine downstream of the RDE. Power extraction from RDCs can be achieved through axial supersonic [12], bladeless [13], or radial outflow turbines [14] and require supersonic flow, or transonic turbines with modified end wall contouring which require subsonic inflow [15]. However, there is still a dearth of information on the optimal design of the passage between combustor and turbine.

Two objectives are outlined in this manuscript. The first objective is to assess heat load, outlet fluctuations, and losses within the coupled combustor and downstream passage. Two different transition passages are analyzed; the first is a supersonic passage that expands flow to \sim Mach 1.6. The second is a subsonic passage suitable for subsonic turbines [16]. The second objective is to determine a strategy to investigate those supersonic and subsonic passages downstream of the combustion region at a reduced computational cost for future optimization of downstream transition elements.

2 Methodology

2.1 Solver Description

CFD++ from Metacomp [17] is employed to solve the URANS equations with a one-step reaction mechanism for stoichiometric H_2 -air [6]. Limitations on the one-step reaction mechanism include the reduced performance at handling for rich mixtures [18]. The solver is a finite-volume density-based solver. Convective fluxes were solved through the Harten-Lax-Van Leer contact approximate Riemann Scheme, and a second Order Total Variation Diminishing (TVD) polynomial interpolation was selected with a continuous limiter. Implicit time-integration with fixed a global timestep of $0.1 \mu s$ was established with an internal iteration termination criterion of 0.1, an essential parameter for unsteady flows [19]. Time step and grid spacing were chosen according to [20] to achieve grid independence. The turbulence closure is provided by the k-omega SST model and based on previous validation in a high-speed environment [13]. Validation of the solver is presented in the appendix for a supersonic shock boundary layer interaction [13] and against coherent anti-Stokes Raman scattering (CARS) thermometry experiments at the exhaust of the Turbine High-pressure Optical RDC [21].

2.2 Investigated Passages Geometries

The two different downstream passages are depicted in Fig. 1 and share the same injection geometry as the experimental counterpart described in [22]. This diverging geometry (Fig. 1a) was inspired by previous work to optimize nozzles for supersonic flows [23] and installed in the Purdue Turbine High-pressure Optical RDC [22]. The diverging geometry has an outlet-to-inlet area ratio of 1.6, measured downstream of the backward-facing step. Figure 1b shows a converging-diverging passage, with a throat suitable for a mass flow averaged Mach number of 1.2 upstream of the throat and decelerate the flow to Mach 0.6 downstream of the throat (outlet-to-inlet area = 1.2). Simulation time for one geometry was three weeks on five nodes with two 10-core Intel Xeon-E5 processors.

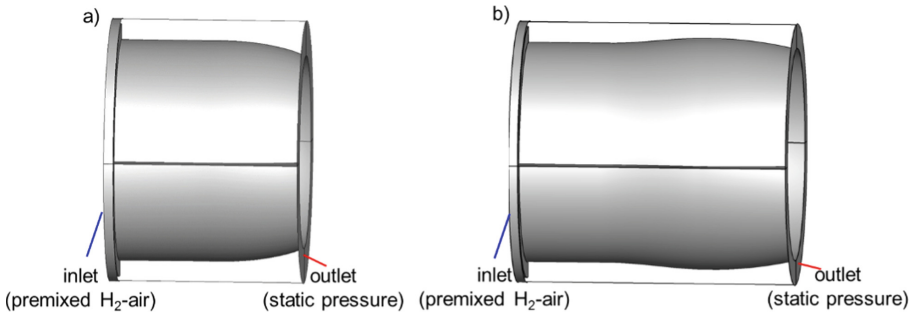


Fig. 1. Selected rotating detonation combustor with two different passages: a) diverging geometry, b) converging-diverging geometry

3 Aerothermal Characterization

3.1 Aerothermal Characterization Within the Transition Passage

This section describes the phenomena occurring within the coupled combustor (region defined by the detonation wave) and downstream passage (through which one or more oblique shocks travel). The pressure contour of the combustor and passage is depicted in Fig. 2a.

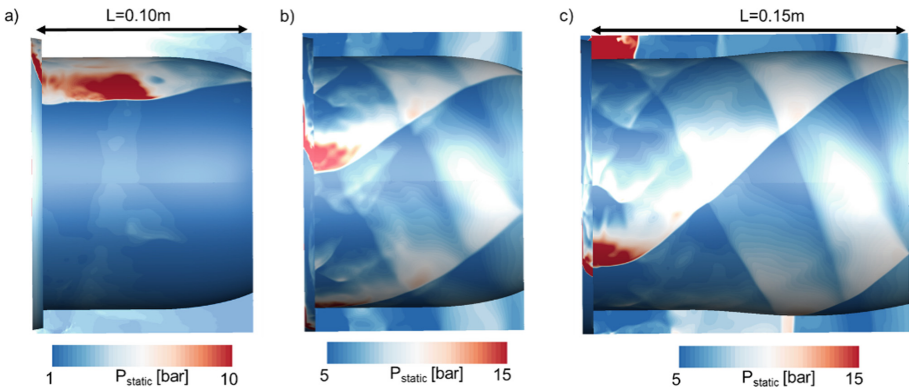


Fig. 2. Static pressure flow field of a) low back pressured RDC with diverging nozzle, b) high back pressured RDC with diverging geometry, c) high back pressured RDC with converging-diverging geometry

A low back pressure (1 bar) and an inlet total pressure of 10 bar and 290K for the premixed reactants were imposed to achieve the required pressure ratio for supersonic exit conditions. Exit conditions are expected to be supersonic and required for supersonic axial, radial, or bladeless turbine designs and will be highlighted in the next section. The same combustor and passage geometry is highlighted in Fig. 2b, but with the outlet pressure increased to 7 bar to model the downstream turbine's effect/blockage. The

selected back pressure was chosen to account for a maximum Mach number of 0.6 at the passage's outlet, suitable for accommodating optimized stator end walls such as those proposed by Liu et al. [16]. Plotted in Fig. 2c, the third one depicts the combustor with a long converging-diverging passage (length 0.15 m).

The pressure contour for the back pressured RDCs indicate several reflective shocks occur within the passage with three reflective waves for the converging-diverging diffuser in contrast to the low back pressured RDC in which continuous expansion occurs. Furthermore, the detonation region is significantly shortened for the higher backpressure device. The combustion occurs immediately downstream of the backward-facing step, with all combustion occurring roughly 0.02 m downstream of the backward-facing step and extending to up to 0.05 m for the supersonic passage. Besides, the converging-diverging geometry features three detonation waves at this condition, while the diverging passage supports four detonation waves at increased backpressure. Local separation occurred tangentially upstream of the shock in the low momentum region.

For cooling estimates, convective heat fluxes are calculated through a simulation with isothermal wall boundary conditions (the walls' temperature was set at 800K). The convective heat flux allows for the scaling of heat flux estimates for a range of wall temperatures. Figure 3 plots the instantaneous convective heat flux ($h = \frac{Q}{T_g - T_{wall}}$) of the supersonic nozzle coefficient, more specifically the unwrapped shroud end wall (a) and hub end wall (b) with a wall temperature of 800K and a gas total temperature of 2300K, corresponding to the mass flow averaged total temperature at the exit of the passage). The detonation wave travels across both end walls in the supersonic passage, with maximum convective heat flux coefficients found tangentially downstream of the detonation wave. The diverging supersonic passage features two detonation waves and is visualized by two high heat flux regions.

Figure 3c,d depict the convective heat flux coefficient of the unwrapped converging-diverging subsonic passage with a wall temperature of 800K and a gas temperature of 2200K (mass flow averaged outlet total temperature). Maximum heat fluxes are observed within the detonation front for the shroud (Fig. 3c), whereas the hub (Fig. 3d) features a more constant convective heat flux as the detonation wave rides across the shroud (Fig. 3c).

The spanwise-averaged convective heat flux for the supersonic nozzle is around 2000 W/K/m² with higher values on the hub end wall than the shroud end wall and decreases towards the outlet to 1000 W/K/m² (Fig. 4). Peak heat fluxes are retrieved at around 0.04 m for the supersonic combustor passage, which lies in the aft part of the combustion region. The spanwise integrated heat flux coefficient indicates that the hub and shroud have similar heat loads, with 94 kW for the hub and 100 kW for the shroud. The required coolant heat load to keep the end walls at 800K is 200 kW.

In contrast to the supersonic passage, the convective heat flux coefficient for the converging-diverging downstream of the combustion region remains constant at about 2000 W/K/m² before decreasing downstream of the throat. Higher heat fluxes are noted in the combustion region compared to the supersonic case due to the higher operating static pressure. Additional cooling is required for longer diffusing passages.

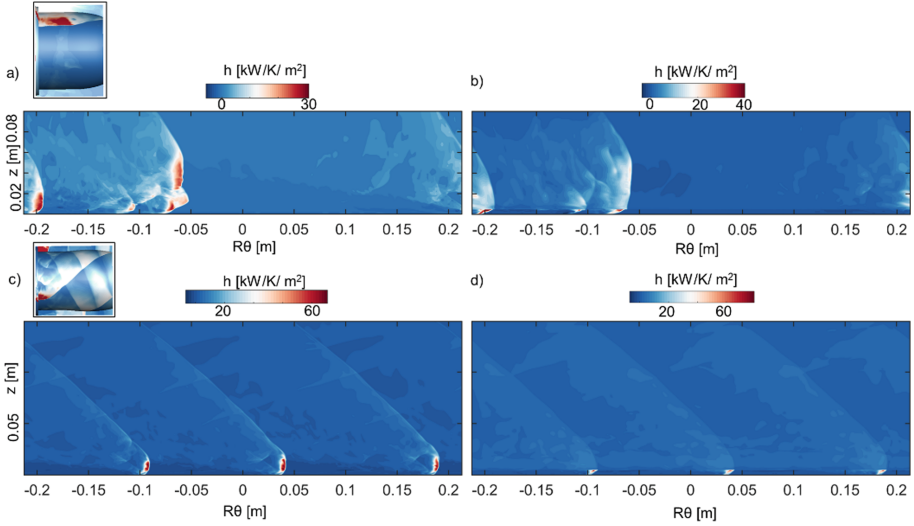


Fig. 3. Instantaneous convective heat flux coefficient for the supersonic passage on the shroud (a), hub (b), and for the subsonic passage with converging-diverging passage shroud (c) and hub (d)

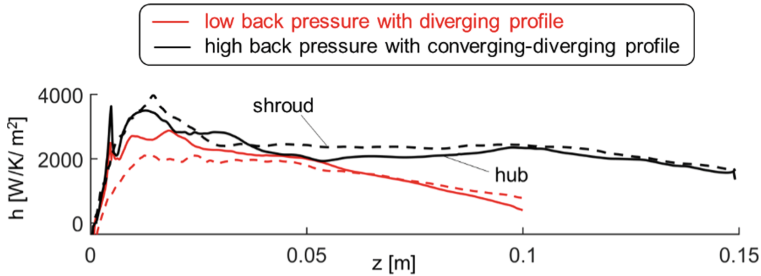


Fig. 4. Average convective heat flux for the diverging geometry and converging-diverging geometry

3.2 Spatio-Temporal Evolution at the Outlet of the Passage

Figure 5a plots the radial mass flow averaged outlet Mach number across the spanwise location (θ). The results demonstrate that the desired supersonic exit conditions for the diverging geometry (solid lines) are indeed achieved for high mass flows, with a mass flow averaged Mach number at the exit of around 1.65. In contrast, the mass flow averaged Mach number for the high back pressured RDC is 0.29 for the diverging passage and 0.36 for the converging-diverging passage. The converging-diverging passage features higher peak Mach numbers of 0.6 due to a lower area passage ratio compared to the diverging passage. Mach numbers of only 0.4 are reached for the diverging geometry at increased backpressure, owing to the more extensive diffusion for the diverging geometry. Mach number is below 0.1 tangentially upstream of the shock, caused by mainly stagnant swirling flow moving at the speed of the oblique shock. In terms of flow angle (Fig. 5b),

tangentially downstream of the oblique shock, flow angles of 20° are present in the supersonic passage. In the low momentum region, the flow angles decrease to -20° . The high back pressured devices have significantly higher flow angles downstream of the shock ($\sim 40^\circ$) than the supersonic passage. Although those maximum flow angles are similar and dictated by the oblique shock, the flow angle decay differs between the two passages, with higher flow angle decay for the diverging passage than the converging-diverging passage, owing to the difference in deceleration through the geometry. The drop in flow angle encircled by region “1”, spans approximately 50° , and flow angle varied from 40° to -30° for the diverging passage, while this only decreased to $\sim -5^\circ$ for the converging-diverging passage (called region “2”). This region contains the highest energy and is computed by the local total enthalpy ($\dot{m}H_{\text{total}}$), visualized in Fig. 5c. Peak enthalpy resides tangentially downstream of the rotating shock. The red line depicts the mass-flow averaged total enthalpy ($\dot{m}H_{\text{total}}$), and 50% of the flow’s total energy is contained within 25% of the circumference for the supersonic passage. For both backpressure cases, 50% of the energy is contained within 33% of the span, slightly above the supersonic passage. The region tangentially downstream of the shock features low momentum/enthalpy with locally negative values tangentially upstream of the shock. The precise identification of regions with high enthalpy is critical for the nozzle guide vane inlet metal angle selection. The radially mass flow averaged total pressure (Fig. 5d) indicates lower local total pressures due to expansion at the exit of the supersonic passage. The total pressure fluctuations are 160% (min-to-max) of the mass flow averaged value for the supersonic passage. In contrast, the converging-diverging geometry features a fluctuation of $\sim 100\%$ (min-to-max) within the high enthalpy region.

Table 1 summarizes the mass flow averaged values and standard deviation of Mach number, flow angle, pressure, and temperature to model the fluctuations emanating from a supersonic passage to a supersonic turbine configuration or from a subsonic passage as an inlet to transonic turbine configuration. The fluctuations of pressure and temperature are significantly lower for the subsonic passage compared to the supersonic passage. To accurately capture the fluctuations, however, the spatio-temporal profile is required, as shown in Fig. 5.

3.3 Impact of the Back Pressure on Pressure Gain

The impact of the back pressure on the losses of the combustor-passage is plotted in Fig. 6 as a function of the mass-flow averaged Mach number and total pressure loss at the passage’s outlet. For low back pressured devices (required for supersonic bladed and bladeless concepts), Mach numbers can reach up to Mach 1.65 for a diverging geometry at the expense of a total pressure loss of 55% for this injector geometry. A significant pressure loss occurs through the injection, with a drop of about 20% downstream of the backwards-facing step. For high back pressured devices, the mass flow averaged Mach number decreases with a consequent reduction in total pressure loss at the exit of the passage (around 20%). Kaemming and Paxson [24] observed similar phenomena in which pressure gain was increased for higher back pressured devices for a fixed injection geometry due to the lower flow speeds across the passage.

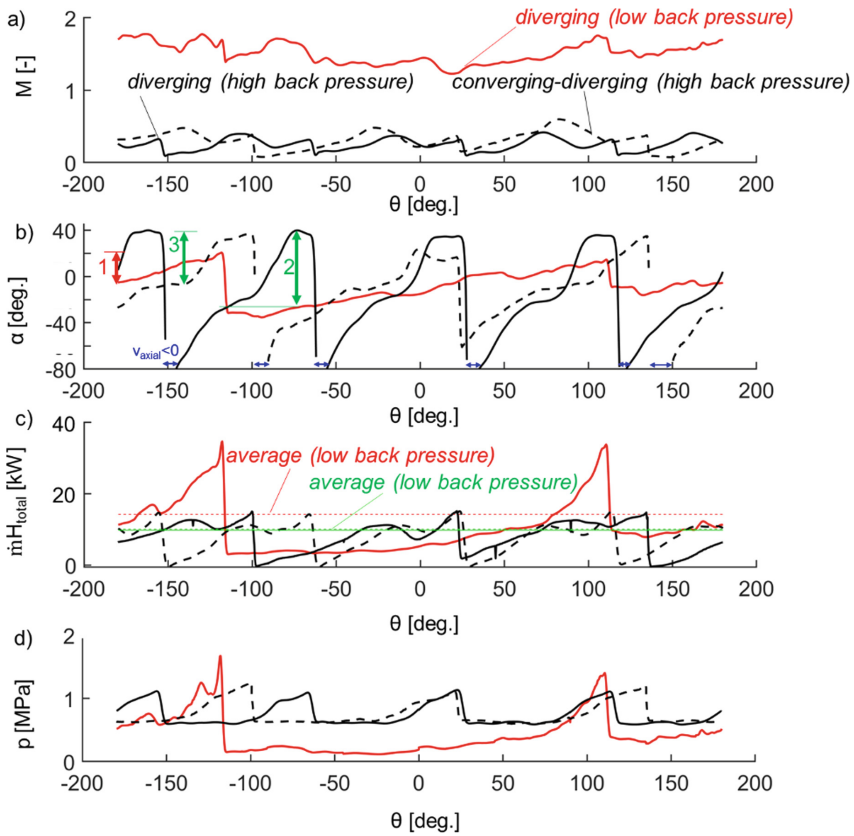


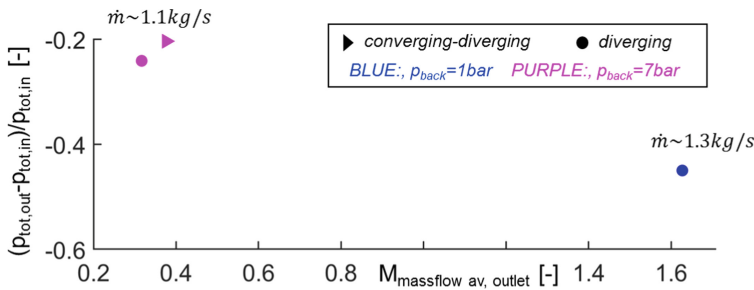
Fig. 5. Radially mass flow averaged quantities as a function of the span at the outlet of the passage: a) Mach number, b) flow angle, c) $\dot{m}H_{\text{total}}$ c) and d) total pressure

3.4 Pressure Loss Across the Transition Passage

The total pressure drop attributed to the supersonic or subsonic passage is investigated by isolating the passage downstream of the combustion zone. This is 0.025 m for the diverging subsonic passage, 0.03 m for the converging-diverging subsonic passage, and 0.065 m for the supersonic passage, as sketched in Fig. 7a. The total pressured drop across the supersonic passage is around 13%, and this pressure drop is dependent on the oblique shock strength and rotational speed. Figure 7b plots the pressure drop as a function of axial length for the isolated passage with similar total pressure drops for the two subsonic passages but with a different decay due to the difference in length and curvature. The pressure drop for the converging-diverging passage is around 25%. Interestingly, the pressure loss decay of all passages is similar. Table 2 summarizes the losses of the respective passages.

Table 1. Mass-flow averaged characteristics with their standard deviation

geometry	$M_{\text{massflow av.}}$	M_{STD}	$\alpha_{\text{massflow av.}}$ [deg]	α_{STD} [deg]
supersonic (diverging)	1.6	~ 0.17	-2	15
subsonic (diverging)	0.29	~ 0.08	-1.01	~ 39
Subsonic (converging-div)	0.36	~ 0.13	-1.44	~ 34
	$p_{s, \text{std.}}/p_{s, \text{massflow av.}}$		$T_{\text{std.}}/T_{s, \text{massflow av}}$	
supersonic (diverging)	$\sim 50\%$		$\sim 13\%$	
	$p_{0, \text{std.}}/p_{\text{massflow av.}}$		$T_{0, \text{std.}}/T_{\text{massflow av}}$	
subsonic (diverging)	$\sim 22\%$		$\sim 4.7\%$	
subsonic (converging-div)	$\sim 22.4\%$		$\sim 4.8\%$	

**Fig. 6.** Total pressure gain as a function of mass flow averaged Mach number for the investigated geometries

4 Assessment of the Chemistry Effects Across the Passage

4.1 Passage Inlet Profile Defined by the Combustor

The inlet of the transition elements is visualized in Fig. 8 as a function of the span to allow for its precise characterization. The location was determined based on the maximum mass-flow averaged total temperature, which occurred at an axial location of 0.025 m downstream of the combustor inlet for the diverging subsonic passage, 0.03 m for the converging-diverging subsonic passage, and 0.065 m for the diverging supersonic passage. Due to the higher expansion occurring in the supersonic passage, a lower total pressure plateau is reached; however, peak total pressures for the three passages are similar (around 20 bar).

Higher maximum total temperatures are achieved for the supersonic profile, compared to the two subsonic passages (Fig. 8b), which could be attributed to the difference

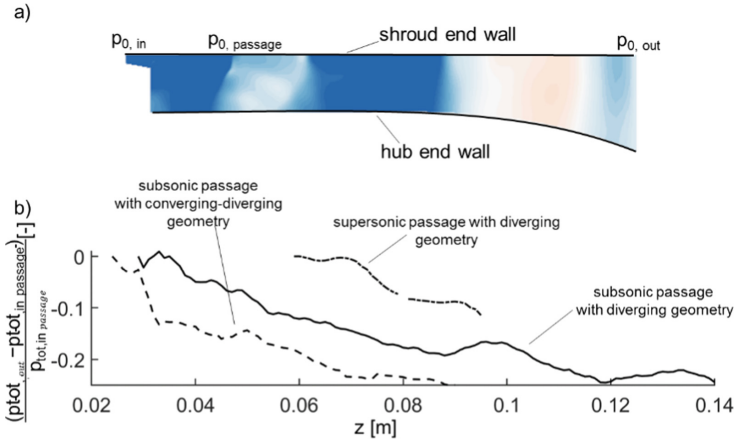


Fig. 7. a) Cross-section of the combustor-passage, and b) mass flow averaged total pressure loss across the isolated passage downstream of the combustion region

Table 2. Summary of the pressure losses for the isolated passages

	Subsonic passage (diverging geometry)	Subsonic passage (diverging geometry)	Subsonic passage (converging-diverging geometry)
Passage length without combustion	0.04 m	0.12 m	0.075 m
Pressure loss across the passage	12%	24.4%	25%

in static temperature upstream of the reactants ahead of the detonation with averaged injection speeds around Mach 1 and 240K of static temperature. By contrast, in the supersonic passage reactants travel at Mach 1.7 with static temperatures of 180K. The Mach number (Fig. 8c) is significantly higher for the supersonic passage, indicative of the combustion process occurring at high flow speeds. From the total enthalpy ($\dot{m}H_{total}$, Fig. 8e), 50% of the flow enthalpy lies within 31% of the span for the subsonic passage and is similar to the passage exhaust profile. In comparison, this is 22% for the supersonic passage. The maximum flow angle (Fig. 8d) for the subsonic passage is between 20° and 30° , while the supersonic passage is 40° . Consequently, flow angles decrease throughout the supersonic passage while they increase for the subsonic passage. Local regions with flow angles below -90° are found caused by areas of reversed flow.

Table 3 shows the mass flow averaged values sampled downstream of the combustion region. Compared to the subsonic passages, the supersonic passage features the highest total enthalpy (computed with an averaged specific heat, c_p , 1700 J/kgK).

Finally, this information is employed to model and isolate the transition passage between combustor and turbine without chemistry, as sketched in Fig. 9. The onset and boundary conditions of the non-reacting passage depend on the backpressure. Modeling

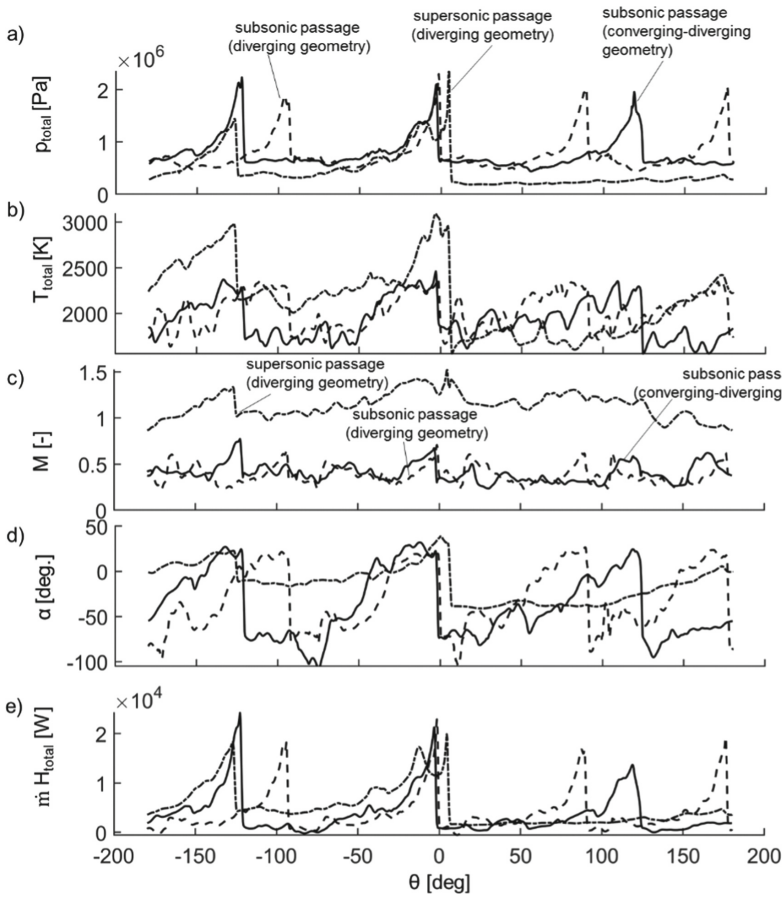


Fig. 8. Radially mass-flow averaged profiles downstream of the combustor and at the inlet of the transition passage: a) total pressure, b) total temperature, c) Mach number, d) flow angle, e) $\dot{m}H_{total}$ [28]

Table 3. Mass flow averaged inlet characteristics and total enthalpy at the onset of the non-reactive passage

	M [-]	α [deg]	p_0 [bar]	T_0 [K]	$\dot{m}H_{total}$ [MW]
Supersonic passage (diverging)	1.17	-3.2	6.3	2300	5.13
Subsonic (diverging)	0.44	-6.9	10.4	2130	3.71
Subsonic (converging-diverging)	0.47	-9.14	10.6	2070	3.97

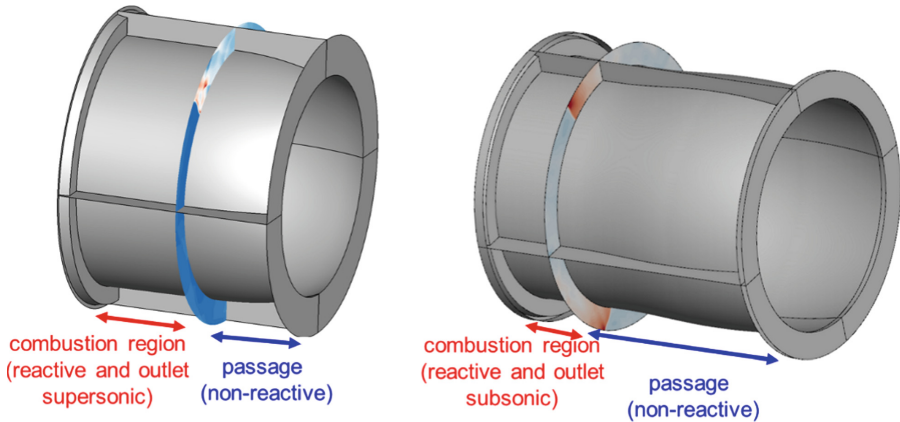


Fig. 9. Numerical domain for the supersonic passage (left) and the subsonic passage (right)

of isolated accelerating passages for RDCs has already been discussed in [23]. Schwer employed a similar method for modeling the plenum upstream of the RDC [25], and Rankin et al. modeled a converging-diverging nozzle to reduce the periodic fluctuations [26].

4.2 Simulation of the Supersonic Passage Without Chemistry

Figure 10a presents the boundary conditions to define the supersonic passage and consist of static pressure, a static temperature, an axial and tangential velocity which are functions of space and time. Those profiles are applied in a ‘passage only’ simulation (Fig. 10b); this approach was already successfully used [27]. In Fig. 10c the mass flow averaged total pressure loss within the passage from the three-dimensional URANS simulation without chemistry is compared to the reactive simulation of the combustor with comparable pressure loss decay rate over the axial distance.

4.3 Simulation of the Isolated Diffusing Passage Without Chemistry

For the subsonic passage, the total pressure, total temperature, and velocity direction (flow angles) downstream of the combustion region of the reactive simulations are imposed as a total pressure and temperature profile with flow angle profile (unsteady in time and space) in a non-reactive unsteady three-dimensional simulation. This non-reactive simulation (with ~6 million grid points) has a calculation time of around 48 h on two High-Performance nodes (Intel Xeon-E5 processors) compared to the coupled simulations, which require about 500 h on six High-Performance nodes. The contours of Fig. 11a,b,c represent the boundary conditions at the inlet interpolated on a 27 (radial) by 1200 grid. This fine interpolation allows an accurate rebuilt of the combustor outlet profile.

The mass flow averaged total pressure is extracted at each axial location. A 25% mass flow averaged total pressure decrease was measured throughout the passage, comparable

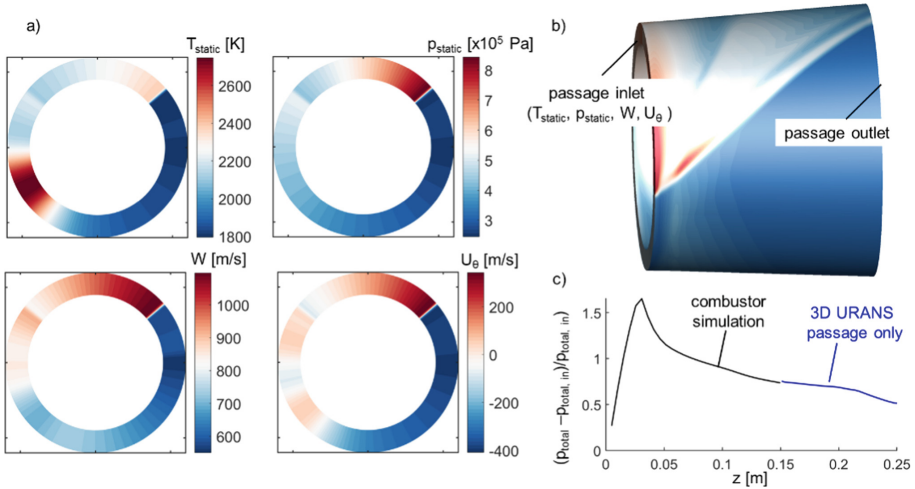


Fig. 10. Modeling of supersonic passage without chemistry: a) inlet boundary conditions, b) numerical domain with pressure signature, c) total pressure loss across the combustor via chemistry simulation, and the passage only simulation without chemistry

to the simulations with combustion (Fig. 11d). Additionally, the temporal evolution at three distinct axial locations from the 3D URANS with chemistry was added, indicating that the subsonic passage simulation without chemistry is within 2% of the combustor-diffuser simulations. The mass-flow averaged Mach number (Fig. 11e) at the subsonic passage outlet decreased from 0.37 to 0.32, and although local variations occur in the diffuser-only simulations, the outlet conditions were matched.

5 Conclusion

We propose design considerations through a multi-pronged approach to assess and model the high-speed transition elements downstream of the combustion region of a rotating detonation combustor. This requires the estimated pressure ratio across the combustor and transition element to assess flow characteristics, loss, and heat flux across combined combustor and transition elements. Second, we dissect the outlet conditions of the passage in terms of Mach number, flow angle, total pressure, and local enthalpy content, which are the four critical input parameters for the turbine design. The final step consists of modeling the transition passage through fast simulations without chemistry by imposing static quantities and velocities for a supersonic passage, or total conditions and flow angles for a subsonic passage based on one expensive reactive simulation.

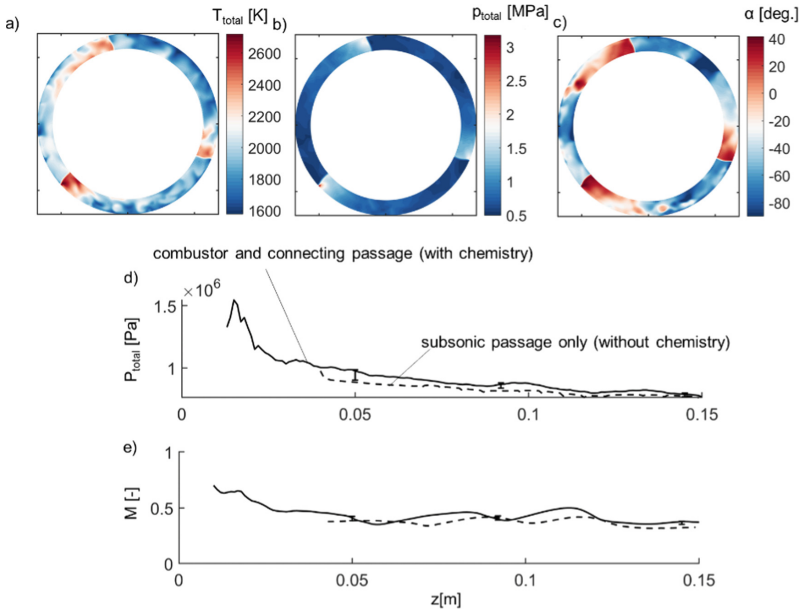


Fig. 11. Verification of the subsonic passage without chemistry vs. the 3D URANS with chemistry for the converging-diverging geometry: a) total inlet temperature, b) total inlet pressure, c) flow angle, d) mass-flow averaged pressure drop along the axial length, e) mass-flow averaged Mach number along the axial length [28].

Specifically, a supersonic passage with a target Mach number of 1.6 and two subsonic passages with an outlet Mach number of 0.6 are analyzed, both with the injector from Purdue’s Turbine High-Pressure Optical RDC. The combustors are characterized through three-dimensional unsteady Reynolds Averaged Navier Stokes (URANS) simulations for a stoichiometric hydrogen-air mixture with a one-step reaction mechanism. We observed that the combustor pressure ratio significantly altered the combustion. Low back pressures resulted in a supersonic passage for diverging geometries, with the combustion zone covering 60% of the passage length. This resulted in complete supersonic flow across the span. The combustion zone was reduced to 20% for the subsonic passage with higher backpressure, and mass-flow averaged Mach numbers of around 0.32 were obtained. Significant differences were observed for the different passages concerning the peak Mach numbers and flow angle variation in the flow’s high enthalpy region. The total pressure drop throughout the isolated subsonic passage downstream of the combustion region without chemistry was 25%, while this was around 12% for the nozzle, although decay rates were similar. The pressure drop across the injector and combustion zone was higher for the supersonic passage, resulting in an overall more considerable total pressure loss. The total pressure, total temperature, and flow angle profile at the exit of the combustor for the two subsonic passages with the same combustor inlet-to-outlet pressure ratio shared similar features. Those profiles were imposed for the isolated subsonic passage without chemistry. A similar mass flow averaged total pressure signature across the axial length was obtained, with a tenfold reduction in computational time

[28]. This method, independent of the actual passage geometry, can be used to optimize the transition element.

Appendix

See Fig. 12.

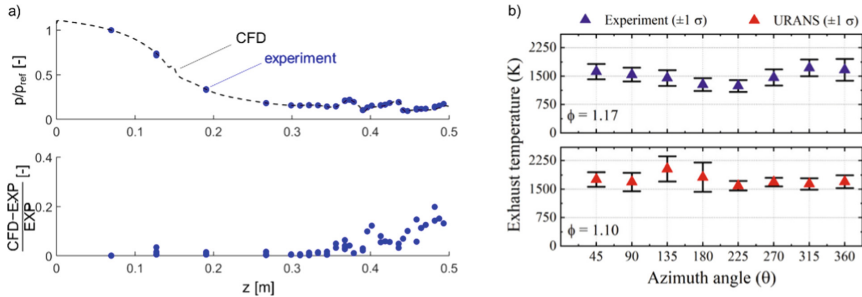


Fig. 12. a) Wall pressure signature (CFD vs. experiment) for Mach 2 supersonic wavy surface [13], b) experiments (top) vs. 3D URANS (bottom) temperature measurements at the exit of the THOR RDC [21]

References

- Roy, A., Bedick, C.R., Ferguson, D.H., Sidwell, T., Strakey, P.A.: Investigating instabilities in a rotating detonation combustor operating with natural gas–hydrogen fuel blend—effect of air preheat and annulus width. *J. Eng. Gas Turbines Power* **141**(11) (2019)
- Braun, J., Saracoglu, B.H., Paniagua, G.: Unsteady performance of rotating detonation engines with different exhaust nozzles. *J. Propuls. Power* **33**(1), 121–130 (2017)
- Anand, V., Gutmark, E.: Rotating detonation combustors and their similarities to rocket instabilities. *Prog. Energy Combust. Sci.* **73**, 182–234 (2019)
- John, Z.M., et al.: Recent progress, development trends, and consideration of continuous detonation engines. *AIAA J.* 1–59 (2020)
- Schwer, D., Kailasanath, K.: Numerical investigation of the physics of rotating-detonation-engines. *Proc. Combust. Inst.* **33**(2), 2195–2202 (2011)
- Frolov, S.M., Dubrovskii, A.V., Ivanov, V.S.: Three-dimensional numerical simulation of the operation of a rotating-detonation chamber with separate supply of fuel and oxidizer. *Russ. J. Phys. Chem. B* **7**(1), 35–43 (2013)
- Cocks, P.A.T., Holley, A.T.: High Fidelity Simulations of a Non - Premixed Rotating Detonation Engine, pp. 1–18 (2016)
- Pal, P., Xu, C., Kumar, G., Drennan, S.A., Rankin, B.A., Som, S.: Large-eddy simulations and mode analysis of ethylene/air combustion in a non-premixed rotating detonation engine. In: *AIAA Propulsion and Energy 2020 Forum*, pp. 1–12 (2020)
- Sato, T., Chacon, F., White, L., Raman, V., Gamba, M.: Mixing and detonation structure in a rotating detonation engine with an axial air inlet. *Proc. Combust. Inst.* **000**, 1–8 (2020)
- Bach, E., Stathopoulos, P., Paschereit, C.O., Bohon, M.D.: Performance analysis of a rotating detonation combustor based on stagnation pressure measurements. *Combust. Flame* **217**, 21–36 (2020)

11. Asli, M., Stathopoulos, P., Paschereit, C.O.: Aerodynamic investigation of guide vane configurations downstream a rotating detonation combustor. *J. Eng. Gas Turbines Power* (2020)
12. Liu, Z., Braun, J., Paniagua, G.: Characterization of a supersonic turbine downstream of a rotating detonation combustor. *J. Eng. Gas Turbines Power* **141**(3), 031501 (2018)
13. Braun, J., Paniagua, G., Falempin, F., Le Naour, B.: Design and experimental assessment of bladeless turbines for axial inlet supersonic flows. *J. Eng. Gas Turbines Power* **142**(4) (2020)
14. Inhestern, L.B., Braun, J., Paniagua, G., Serrano Cruz, J.R.: Design, optimization, and analysis of supersonic radial turbines. *J. Eng. Gas Turbines Power* **142**(3), 1–12 (2020)
15. Liu, Z., Braun, J., Paniagua, G.: Integration of a transonic high-pressure turbine with a rotating detonation combustor and a diffuser. *Int. J. Turbo Jet-Engines* (2020)
16. Liu, Z., Braun, J., Paniagua, G.: Thermal power plant upgrade via a rotating detonation combustor and retrofitted turbine with optimized endwalls. *Int. J. Mech. Sci.* **188**, 105918 (2020)
17. Chakravarthy, S., Peroomian, O., Goldberg, U., Palaniswamy, S.: The CFD++ computational fluid dynamics software suite. *SAE Tech. Pap. Ser.* **1** (2010)
18. Fernández-Galisteo, D., Sánchez, A.L., Liñán, A., Williams, F.A.: One-step reduced kinetics for lean hydrogen-air deflagration. *Combust. Flame* **156**(5), 985–996 (2009)
19. Saavedra, J., Paniagua, G., Lavagnoli, S.: On the transient response of the turbulent boundary layer inception in compressible flows. *J. Fluid Mech.* **850**, 1117–1141 (2018)
20. Braun, J., Sousa, J., Paniagua, G.: Numerical assessment of the convective heat transfer in rotating detonation combustors using a reduced-order model. *Appl. Sci.* **8**(6), 893 (2018)
21. Athmanathan, V., et al.: “Femtosecond/picosecond rotational coherent anti-Stokes Raman scattering thermometry in the exhaust of a rotating detonation combustor. *Combust. Flame* **231**, 111504 (2021)
22. Athmanathan, V., et al.: Turbine-integrated high-pressure optical RDE (THOR) for injection and detonation dynamics assessment. In: *AIAA Propulsion and Energy 2019 Forum*, pp. 1–15 (2019)
23. Braun, J., Saavedra Garcia, J., Paniagua, G.: Evaluation of the unsteadiness across nozzles downstream of rotating detonation combustors. In: *55th AIAA Aerospace Sciences Meeting*, pp. 1–13 (2017)
24. Kaemming, T.A., Paxson, D.E.: Determining the pressure gain of pressure gain combustion. In: *2018 Joint Propulsion Conference*, p. 4567 (2018)
25. Schwer, D.A., Kaemming, T.A., Kailasanath, K.: Pressure feedback in the diffuser of a ram-RDE propulsive device. In: *55th AIAA Aerospace Sciences Meeting* (2017)
26. Rankin, B.A., Hoke, J., Schauer, F.: Periodic exhaust flow through a converging-diverging nozzle downstream of a rotating detonation engine. In: *52nd Aerospace Sciences Meeting*, pp. 1–12 (2014)
27. Braun, J., et al.: Characterization of an integrated nozzle and supersonic axial turbine with a rotating detonation combustor. In: *AIAA Propulsion and Energy 2019 Forum*, pp. 1–11 (2019)
28. Braun, J., Paniagua, G., Ferguson, D.: Aero-thermal characterization of accelerating and diffusing passages downstream of rotating detonation combustors. In: *ASME Turbo Expo 2021, GT2021–59111*